

One-Pot Synthesis of α -Fe₂O₃ Nanospindles as High-Performance Lithium-Ion Battery Anodes

Yanhua Ding*, Bing Liu*, Rongsheng Cai[†], Tuo Xin*, Chen Li*,
Linhua Xia*[‡] and Yiqian Wang*[§]

*College of Physics, Qingdao University
No. 308 Ningxia Road, Qingdao 266071
P. R. China

[†]School of Physics and Astronomy, University of Birmingham
Birmingham B15 2TT UK

[‡]lhx@qdu.edu.cn

[§]yqwang@qdu.edu.cn

Received 8 October 2017

Accepted 24 January 2018

Published 21 February 2018

Hematite nanospindles with a uniform size of ~ 270 nm in length and ~ 90 nm in width are prepared using a facile one-step hydrothermal method. Polyvinylpyrrolidone (PVP) serves as a structure-directing agent to control the primary morphology and aggregations. When evaluated as anode materials for lithium-ion batteries (LIBs), the electrode of sodium alginate (SA) binder exhibits a much better electrochemical performance than that with the polyvinylidene fluoride (PVDF) binder. Remarkably, the electrode using SA binder can deliver a high reversible specific capacity of $979 \text{ mAh}\cdot\text{g}^{-1}$ after 50 cycles and prominent rate capability. The microstructural evolution of the nanospindles after the electrochemical cycling is investigated by scanning transmission electron microscopy (STEM). Our results may provide important mechanistic insights for the design of nanostructured anode materials for LIBs.

Keywords: α -Fe₂O₃ nanospindles; electrochemical performance; scanning transmission electron microscopy; microstructure; lithium-ion batteries.

1. Introduction

Rechargeable lithium-ion batteries (LIBs) are commonly used as power sources for portable electronic devices.¹ They are also considered as very promising power sources in electric vehicles, hybrid electric vehicles and stationary energy storage systems.^{2–7} The traditional graphite does not meet the

increasing demand for LIBs' anode materials due to its low theoretical specific capacity ($372 \text{ mAh}\cdot\text{g}^{-1}$). To meet the growing demand, it is urgent to develop novel electrode materials with high power/energy density, long cycle life, low cost and high safety.^{8,9} The metal oxides have been adjudged as potential candidates with high theoretical capacity and safety.¹⁰

[§]Corresponding author.

As the most stable iron oxide, hematite ($\alpha\text{-Fe}_2\text{O}_3$) has attracted specific attention because of its high capacity of $1007\text{ mAh}\cdot\text{g}^{-1}$, its non-toxicity, low cost, as well as its abundance.^{11–14} Nevertheless, the implementation of $\alpha\text{-Fe}_2\text{O}_3$ in commercialized anode is obstructed by significant volume expansion and poor electrical conductivity, which can drastically affect its performance.¹⁵ Tremendous efforts have been devoted to the synthesis and research of Fe_2O_3 . Numerous efforts have been directed towards nanostructural engineering to improve the $\alpha\text{-Fe}_2\text{O}_3$ anode performance by reducing the particle size,¹⁶ developing one-dimensional (1D) nanorods,¹⁷ two-dimensional (2D) nanosheets¹⁸ and three-dimensional (3D) hollow or porous structures^{19–22} and coating $\alpha\text{-Fe}_2\text{O}_3$ with carbon.^{23,24} Among the various methods and structures, the hydrothermal method is simple and feasible, and the spindle-like structure is more appropriate for LIBs because the 1D structure is beneficial for charge transfer. In addition, the research has implied that the size of the particle can impact its electrochemical performance. Zou *et al.* synthesized Fe_2O_3 -graphene nanocomposites by microwave-assisted hydrothermal method.²⁵ The obtained spindle-like composite with a length of $\sim 200\text{ nm}$ delivered a capacity of $734\text{ mAh}\cdot\text{g}^{-1}$ after 40 cycles at $100\text{ mA}\cdot\text{g}^{-1}$, while the particle-like composite with a size of $\sim 80\text{ nm}$ delivered a capacity of $312\text{ mAh}\cdot\text{g}^{-1}$ after 40 cycles at $100\text{ mA}\cdot\text{g}^{-1}$.²⁵ Xu *et al.* prepared spindle-like $\alpha\text{-Fe}_2\text{O}_3$ by a two-step calcinations method.²⁶ The as-prepared spindle-like mesoporous $\alpha\text{-Fe}_2\text{O}_3$ with a length of $\sim 800\text{ nm}$, exhibited a reversible capacity of $911\text{ mAh}\cdot\text{g}^{-1}$ after 50 cycles at 0.2 C .²⁶ Although these techniques have significantly improved the electrochemical performances of $\alpha\text{-Fe}_2\text{O}_3$, they are complicated to realize and the materials have a relatively low specific capacity and poor cycling stability. Therefore, it is worthwhile exploring $\alpha\text{-Fe}_2\text{O}_3$ nanospindles with better performance by a facile and economical synthesis method.

Recently, lots of studies have shown that the binder is a crucial component of battery. The aqueous binders with carboxy groups display better electrochemical properties than the commonly-used polyvinylidene fluoride (PVDF).^{27,28} Sodium alginate (SA) may be the suitable binder due to the carboxylic groups' even distribution and sufficient polar functional groups in the polymer chain. Particularly, the electrode with SA binder exhibited a

good cycling stability and capacity retention in the case of alloying electrodes such as Si and Sn.^{29,30} However, little work is focused on the $\alpha\text{-Fe}_2\text{O}_3$ electrode with the SA binder. Herein, we propose a strategy of combining active-material nanostructures and aqueous binder to obtain an optimum lithium storage performance. The active materials, $\alpha\text{-Fe}_2\text{O}_3$ nanospindles, were fabricated using a facile one-step hydrothermal method in the presence of polyvinylpyrrolidone (PVP), followed by a subsequent annealing treatment. The obtained $\alpha\text{-Fe}_2\text{O}_3$ nanospindles with SA binder as an anode exhibit a high reversible capacity of $979\text{ mAh}\cdot\text{g}^{-1}$ after 50 cycles at $100\text{ mA}\cdot\text{g}^{-1}$, whereas for the same active materials with PVDF binder, the capacity drops to less than $600\text{ mAh}\cdot\text{g}^{-1}$ after 50 cycles. Remarkably, $\alpha\text{-Fe}_2\text{O}_3$ nanospindles used the SA binder to deliver high capacities of $560\text{--}750\text{ mAh}\cdot\text{g}^{-1}$ at a high rate of $1\text{--}2\text{ A}\cdot\text{g}^{-1}$, indicating a remarkable rate capability. The morphology of $\alpha\text{-Fe}_2\text{O}_3$ nanospindles with SA binder after the electrochemical cycling process was investigated by scanning transmission electron microscopy (STEM).

2. Experimental

2.1. Materials preparation

$\alpha\text{-Fe}_2\text{O}_3$ nanospindles were synthesized by a hydrothermal method. Typically, 1 mmol of $\text{FeCl}_3\cdot 6\text{H}_2\text{O}$, 0.6 g PVP, 6 mL ethylenediamine were dissolved in 30 mL deionized water and 30 mL ethanol under stirring for 30 min . Thereafter, the mixture was transferred into a 100 mL teflon-lined stainless-steel autoclave and heated at 180°C for 6 h . After the autoclave was cooled down to room temperature naturally, the red precipitates were centrifuged and washed with deionized water and ethanol several times, and then dried in an oven at 60°C overnight. Finally, the dried powders were further calcined at 500°C for 2 h in a nitrogen atmosphere to obtain $\alpha\text{-Fe}_2\text{O}_3$ nanospindles. For comparison, the bulk $\alpha\text{-Fe}_2\text{O}_3$ was fabricated under the same conditions in the absence of PVP and ethylenediamine.

2.2. Materials characterization

The crystallographic information and composition of the samples were investigated by x-ray diffraction (XRD, Rigaku SmartLab) with $\text{Cu-K}\alpha$ radiation ($\lambda = 0.154\text{ nm}$) with 2θ ranging from 20° to 80° .

The morphologies and the microstructures of the products were characterized by field-emission scanning electron microscopy (FESEM, Hitachi S-4800) and STEM (JEOL JEM2100F).

2.3. Electrochemical measurements

Electrochemical measurements were conducted using a half coin-type cell (CR2025) assembled inside a glove box (Mikrouna) under an argon atmosphere at room temperature (25 °C). The working electrode was fabricated by mixing α -Fe₂O₃ nanospindles (70 wt.%), acetylene black (15 wt.%) and SA (15 wt.%) or PVDF (15 wt.%). For the bulk α -Fe₂O₃ electrode, the bulk α -Fe₂O₃, acetylene black and SA binder were mixed with a weight ratio of 70:15:15. Then the mixture was pasted on the copper current collector and dried in a vacuum oven at 120 °C for 12 h. The capacity of the battery was merely based on the weight of Fe₂O₃. Metallic lithium foil was used as a counter electrode, 1 M LiPF₆ in ethylenecarbonate (EC) and dimethyl carbonate (DMC) (EC:DMC = 1:1 in volume) as the electrolyte, and a polypropylene microporous film was used as a separator. The galvanostatic charge/discharge tests were performed on the LAND CT 2001A battery testing system with a voltage range from 0.01 V to 3.0 V versus Li⁺/Li. The cyclic voltammetry (CV) was performed on Metrohm Autolab PGSTAT302N in the potential range of 0.01 V–3.0 V with a scan rate of 0.1 mV·s⁻¹. Electrochemical impedance spectroscopy (EIS) was performed on fresh cells at open circuit potential with Metrohm Autolab PGSTAT302N by applying a sine wave with an amplitude of 5.0 mV over the frequency range from 100 kHz to 0.01 Hz.

3. Results and Discussion

Both the crystal structure and the phase of prepared samples were investigated by XRD. Figure 1 shows the XRD patterns of products before and after annealing at 500 °C for 2 h in nitrogen. All the detected diffraction peaks confirm the high crystallinity of the products, which can be assigned to a hexagonal structure α -Fe₂O₃ (JCPDS No. 33-0664).³¹

Figures 2(a) and 2(b) show typical FESEM images of α -Fe₂O₃ nanostructures after annealing, recorded at different magnifications. It clearly reveals that the nanostructures are spindle-like hematites with a relatively uniform size. The

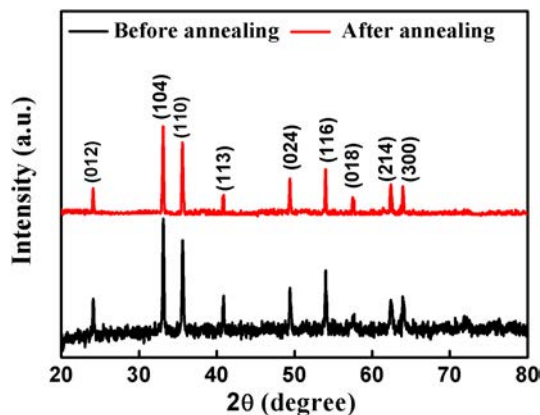


Fig. 1. Typical XRD patterns of the products before and after annealing.

dimensions of the hematite spindles are about 270 nm in length and about 90 nm in width. Figure 2(c) presents a typical bright field (BF) transmission electron microscopy (TEM) image of a single α -Fe₂O₃ nanospindle, whose dimensions are consistent with the FESEM results. Figure 2(d) displays a typical high-resolution transmission electron microscopy (HRTEM) image of an individual nanospindle, from which the (104) lattice spacing is measured to be 2.74 Å, consistent with that of pure α -Fe₂O₃. PVP can control the crystal growth of the hematite by selectively adsorbing Fe³⁺ to form a spindle-like structure, which has already been reported in other materials.³²

The Li⁺ storage performance of the α -Fe₂O₃ nanospindles with SA binder was evaluated by the CV and galvanic charge/discharge. Figure 3(a) is the CV of α -Fe₂O₃ nanospindles measured at applied voltages varying between 0.01–3.00 V. In the first cathodic scan, the small peak located at 1.4 V is caused by the initial lithium insertion into α -Fe₂O₃ ($\text{Fe}_2\text{O}_3 + x\text{Li}^+ + xe^- \rightarrow \text{Li}_x\text{Fe}_2\text{O}_3$, $\text{Li}_x\text{Fe}_2\text{O}_3 + (2-x)\text{Li}^+ + (2-x)e^- \rightarrow \text{Li}_2\text{Fe}_2\text{O}_3$), and the large peak observed at 0.5 V is ascribed to the formation of solid electrolyte interphase (SEI) film, the reduction of α -Fe₂O₃ to Fe and the formation of Li₂O when the Fe₂O₃ phase reacts with Li⁺ ($\text{Li}_2\text{Fe}_2\text{O}_3 + 4\text{Li}^+ + 4e^- \rightarrow 2\text{Fe} + 3\text{Li}_2\text{O}$).³³ This peak located 0.5 V disappears in the following cycles, and another peak is observed at 0.8 V, which is due to the reversible insertion of lithium ions and the complete reduction of Fe³⁺ to Fe(0).³³ In addition, the anodic peak at 1.8 V during the first cycle can be attributed to the oxidation of Fe(0) to Fe³⁺ ($2\text{Fe} + 3\text{Li}_2\text{O} \rightarrow \text{Fe}_2\text{O}_3 + 6\text{Li}^+ + 6e^-$). Little change is found in the following

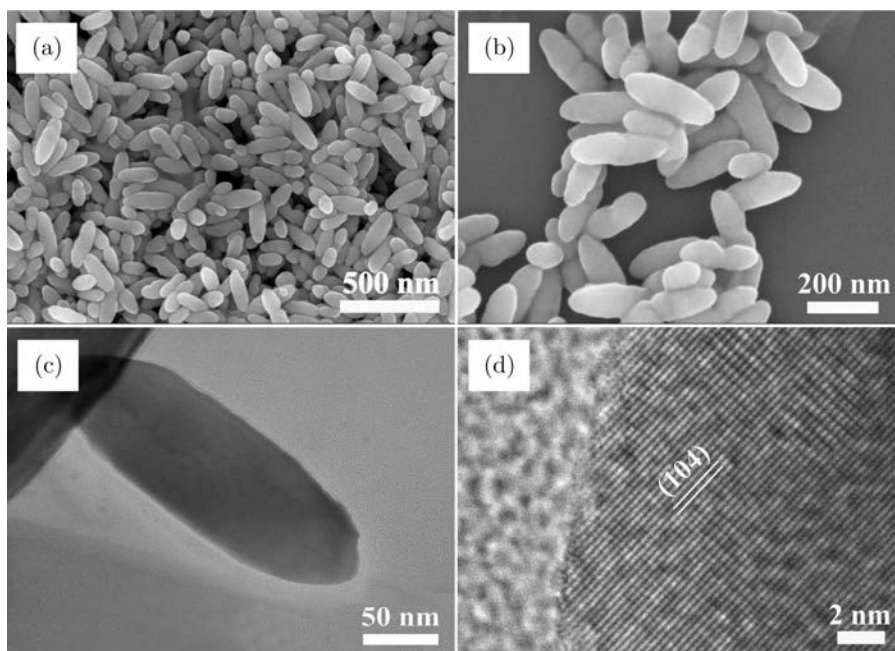


Fig. 2. Typical FESEM images of α -Fe₂O₃ nanospindles (a) and (b), (c) typical BF TEM image of α -Fe₂O₃ nanospindle and (d) typical HRTEM image of α -Fe₂O₃ nanospindle.

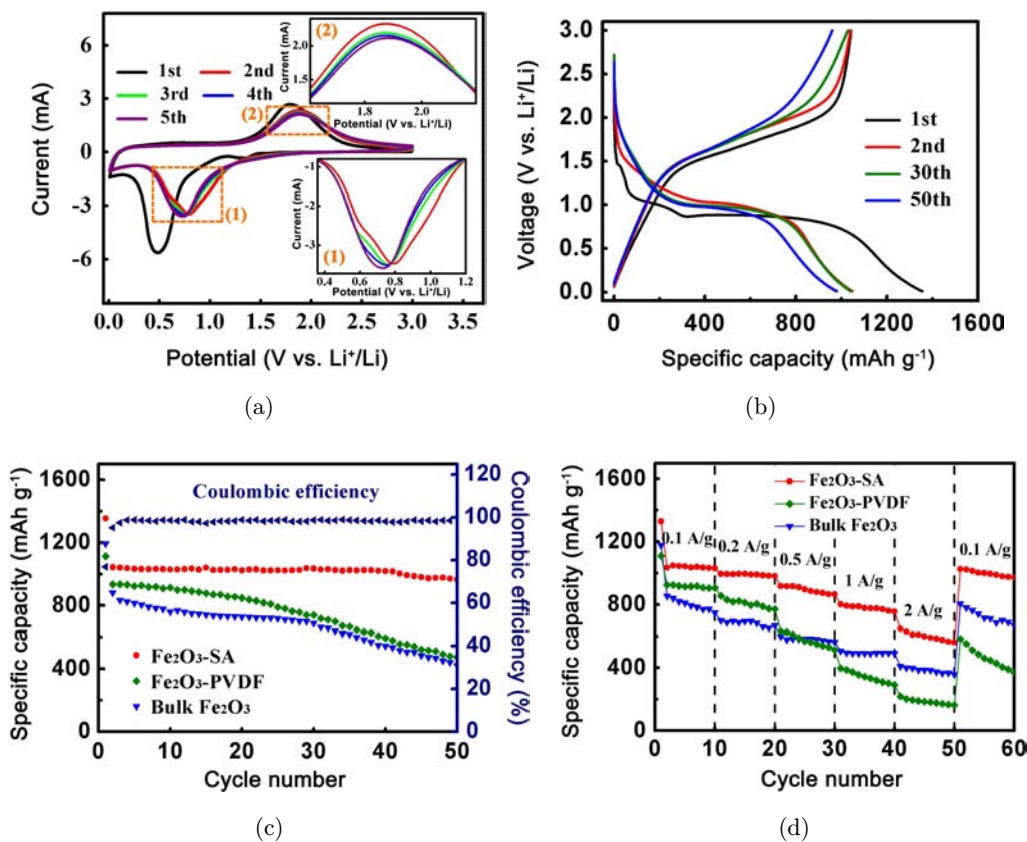


Fig. 3. (a) The CV of the α -Fe₂O₃ nanospindles with SA binder, the insets are the enlarged CV curves, (b) discharge/charge curves of α -Fe₂O₃ nanospindles with SA binder, (c) cycling ability of α -Fe₂O₃ nanospindles with SA and PVDF binders and bulk Fe₂O₃ with SA binder and (d) rate performance of α -Fe₂O₃ nanospindles with SA and PVDF binders and bulk Fe₂O₃ with SA binder.

cycles, which suggests that the electrochemical reaction of α -Fe₂O₃ nanospindles is highly reversible.

Figure 3(b) displays capacity versus voltage curves of α -Fe₂O₃ nanospindles with SA binder (1st, 2nd, 30th, 50th cycles) at 100 mA·g⁻¹. During the first discharge, the voltage platforms are in good agreement with the CV result described above. The charge curve shows a sloping platform at ~2.0 V as a result of reverse reaction.³⁴ The reaction offers a dominant contribution to Li storage capability, leading to a high first-cycle discharge specific capacity of 1354 mAh·g⁻¹. A reversible charge specific capacity is 1032 mAh·g⁻¹, thus the relatively irreversible capacity loss is 23%. The initial irreversible capacity loss results from the formation of SEI on the surface of iron oxide during the first cycle of Li⁺ insertion, as commonly observed in anode materials.³⁴ During the second cycle, the discharge and charge specific capacities are 1060 mAh·g⁻¹ and 1029 mAh·g⁻¹, respectively, which are even higher than the theoretical capacity of α -Fe₂O₃. This phenomenon may be attributed to the formation of polymeric gel-like film resulting from kinetically-activated electrolyte degradation, which has been discovered in other transition metal oxides.³⁵

Figure 3(c) reveals the cycling performances of the α -Fe₂O₃ nanospindles with SA and PVDF binders and bulk Fe₂O₃ with SA at 100 mA·g⁻¹. After 50 cycles, the as-prepared α -Fe₂O₃ nanospindles with SA binder still exhibit a high discharge specific capacity of 964 mAh·g⁻¹. A Coulombic efficiency of ~98% is measured after the 3rd cycle. However, the capacity of the α -Fe₂O₃ nanospindles with PVDF binder and bulk α -Fe₂O₃ with SA binder drastically drops to less than 600 mAh·g⁻¹ after 50 cycles. In addition, α -Fe₂O₃ anode materials were cycled to evaluate the rate performance. As shown in Fig. 3(d), the α -Fe₂O₃ nanospindles deliver specific capacities of 1029, 981, 865, 755, 560 mAh·g⁻¹ at 0.1, 0.2, 0.5, 1 and 2 A·g⁻¹, respectively. A reversible discharge capacity of 1025 mAh·g⁻¹ can be obtained once the current density returns to 0.1 A·g⁻¹ after 50 cycles, which is much higher than those of α -Fe₂O₃ nanospindles with PVDF binder and bulk α -Fe₂O₃ with SA binder. The cycling and rate performances of α -Fe₂O₃ nanospindles are superior to those reported for some iron oxide anode materials. For instance, Bai *et al.* found the reversible capacity of ~920 mAh·g⁻¹ after 40 cycles at 100 mA·g⁻¹ for α -Fe₂O₃ nano-assembled spindles.³⁶ Xiong and co-workers reported that the Fe₂O₃

nanospindles electrode showed a capacity of 921.7 mAh·g⁻¹ at 200 mA·g⁻¹ after 50 cycles,³⁷ and the Fe₂O₃ nanorods electrode delivered a discharge capacity of 761.7 mAh·g⁻¹ at 500 mA·g⁻¹ up to 60 cycles.³⁸ The capacity of the bare α -Fe₂O₃ nanospindles electrode was lower than 200 mAh·g⁻¹ after 50 cycles at 100 mA·g⁻¹.^{39–41} Compared to previous reports, the as-prepared α -Fe₂O₃ with SA binder shows an excellent electrochemical property. The SA tends to dissolve in water, which can obtain a fully-stretched molecular conformation due to the rigid long chains and the electrostatic repulsive interactions. The unique structure makes for uniform 3D networking between the acetylene black and α -Fe₂O₃ nanospindles, which can strengthen electrode architecture.⁴² The carbohydrate-based polymer has a strong cohesive force to bond α -Fe₂O₃ and the Cu foil because of sufficient polar functional groups. However, the electrode with PVDF binder has a poor mechanical strength due to the inadequate connection of the active materials with flexible, coil-shape chains.

To further demonstrate the superior electrochemical performances, EIS measurements were conducted on α -Fe₂O₃ nanospindles with SA and PVDF binders, and α -Fe₂O₃ nanospindles and bulk Fe₂O₃ with SA binder. As shown in Fig. 4, the Nyquist plots are composed of a compressed semi-circle in high frequency and an inclined line in low frequency, respectively, which correspond to the charge transfer process and lithium diffusion process,^{43,44} respectively. The classical equivalent circuits (insets in Fig. 4) are used to model the electrochemical system, in which R_s represents the ohmic resistance, CPE represents the double-layer capacitance, R_{ct} represents the charge transfer resistance, W represents the Warburg impedance describing the lithium diffusion process in composites. As shown in Fig. 4(a), the semicircle for α -Fe₂O₃ nanospindles with SA binder (33 Ω) is smaller than that for α -Fe₂O₃ nanospindles with PVDF binder (65 Ω). The semicircle for α -Fe₂O₃ nanospindles (33 Ω) is smaller than that for bulk α -Fe₂O₃ with SA binder (47 Ω), as displayed in Fig. 4(b). Thus, the α -Fe₂O₃ nanospindles with the SA binder have the lowest charge-transfer impedance.

To understand the electrochemical performance, TEM and STEM were used to investigate the microstructural evolution of the α -Fe₂O₃ nanospindles with SA binder in the lithiated states (0.01 V).

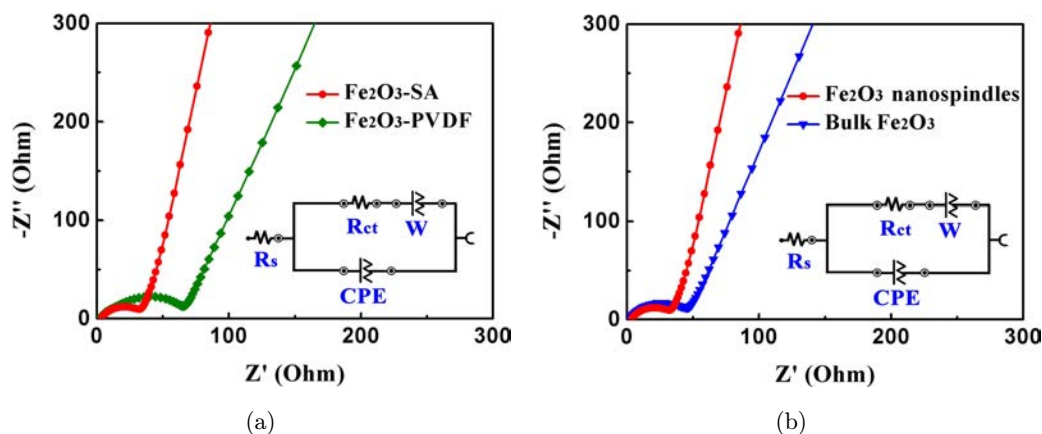


Fig. 4. Nyquist plots of α - Fe_2O_3 . (a) nanospindles with SA and PVDF binders and (b) nanospindles and bulk with SA binder. Insets are the equivalent circuits.

Figures 5(a) and 5(c) are the BF TEM images of α - Fe_2O_3 nanospindles after several discharge/charge cycles. The nanograin morphology of active materials remains in a spindle-like shape after three and 50 discharge cycles, while its length and width are much bigger than those dimensions before cycling, suggesting that a volume expansion takes place. Figures 5(b) and 5(d) show the STEM images of the anode materials in the lithiated states to clearly demonstrate their surface transformation. At the beginning, few particles are observed on the

surfaces of spindle initially after three discharge cycles. Subsequently, the surface of the spindle is covered with small particles and gradually becomes rough. Finally, small amount of nanograins peel off from the surface layer after 50 cycles. Figure 5(e) shows a typical HRTEM image of the active materials after 50 cycles. The lattice spacing of the particle is measured to be 2.05 Å, matching well with the {110} planes of Fe, which provides a direct evidence for the formation of Fe nanocrystals dispersed into the Li_2O matrix during the lithiation process.

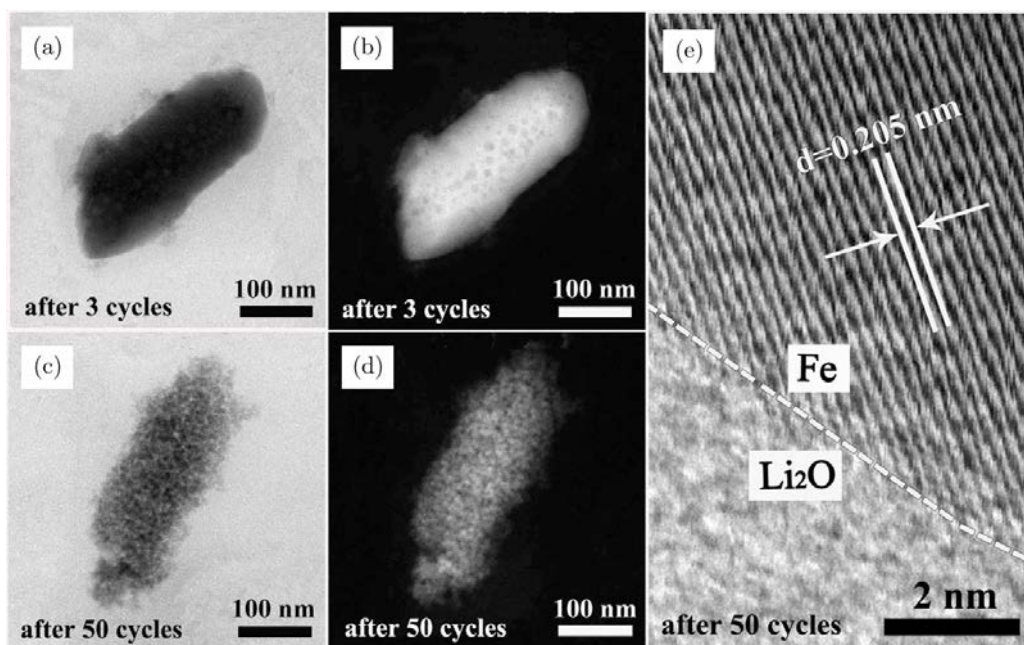


Fig. 5. (a) Typical BF TEM image after three discharge cycles, (b) typical STEM image after three discharge cycles, (c) typical BF TEM image after 50 discharge cycles, (d) typical STEM image after 50 discharge cycles and (e) typical HRTEM image after 50 discharge cycles.

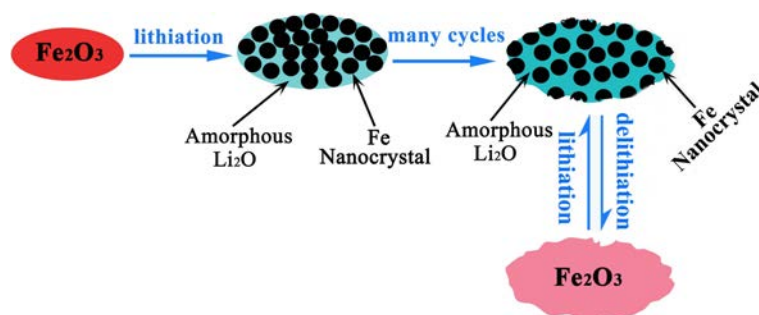


Fig. 6. Schematic illustration for the microstructural evolution of α -Fe₂O₃ during the lithiation/delithiation process.

Figure 6 shows the schematic illustration of the α -Fe₂O₃ nanospindles during electrochemical cycling. During the lithiation process, Li⁺ ions transfer from the metallic lithium to α -Fe₂O₃ electrode through the nonaqueous electrolyte and separator. Li⁺ insertion cycling leads to the volume expansion of α -Fe₂O₃ nanospindles. The lithium storage capacity of α -Fe₂O₃ is delivered through the reversible conversion reaction between Li⁺ and α -Fe₂O₃, forming Fe nanocrystals dispersed in a Li₂O matrix. After several cycles, small amount of nanograins will peel off from the surface layer and the surface gradually becomes rough. The α -Fe₂O₃ nanospindles can keep their original shape after the discharging/charging cycles, which is beneficial for their cycling stability.

4. Conclusions

In summary, homogeneous α -Fe₂O₃ nanospindles have been synthesized by a simple hydrothermal method. With SA as binder, the α -Fe₂O₃ nanospindle electrode exhibits a remarkable cycling performance. The unique spindle structure can reduce the possibility of structure collapse, and the SA binder can avoid peeling from the Cu foil during the electrochemical cycling. The strategy of combining active-material nanostructures with effective binders is extremely rewarding for the development of high-performance LIBs.

Acknowledgments

We would like to thank the financial support from the National Key Basic Research Development Program of China (Grant No. 2012CB722705), the National Natural Science Foundation of China (Grant No. 10974105), the Natural Science Foundation for Outstanding Young Scientist in Shandong Province

(Grant No. JQ201002) and the High-end Foreign Experts Recruitment Programs (Grant Nos. GDW20143500163 and GDW20163500110). Y. Q. Wang would also like to thank the financial support from the Top-notch Innovative Talent Program of Qingdao City (Grant No. 13-CX-08), the Taishan Scholar Program of Shandong Province, Qingdao International Center for Semiconductor Photoelectric Nanomaterials and the Shandong Provincial University Key Laboratory of Optoelectrical Material Physics and Devices.

References

1. R. Marom, S. F. Amalraj, N. Leifer, D. Jacob and D. Aurbach, *J. Mater. Chem.* **21**, 9938 (2011).
2. J. Kim and A. Manthiram, *Nature* **390**, 265 (1997).
3. J.-M. Tarascon and M. Armand, *Nature* **414**, 359 (2001).
4. C. K. Chan, H. L. Peng, G. Liu, K. Mcllwraith, X. F. Zhang R. A. Huggins and Y. Cui, *Nat. Nanotechnol.* **3**, 31 (2008).
5. B. Kang and G. Ceder, *Nature* **458**, 190 (2009).
6. B. Scrosati, J. Hassoun and Y. K. Sun, *Energy Environ. Sci.* **4**, 3287 (2011).
7. V. Etacheri, R. Marom, R. Elazari, G. Salitra and D. Aurbach, *Energy Environ. Sci.* **4**, 3243 (2011).
8. J. N. Zhang, K. X. Wang, Q. Xu, Y. C. Zhou, F. Y. Cheng and S. J. Guo, *ACS Nano* **9**, 3369 (2015).
9. Y. M. Sun, X. L. Hu, W. Luo and Y. H. Huang, *ACS Nano* **5**, 7100 (2011).
10. Z. Y. Wang, S. Madhavi and X. W. Lou, *J. Phys. Chem. C* **116**, 12508 (2012).
11. P. Poizot, S. Laruelle, S. Grugeon, L. Dupont and J.-M. Tarascon, *Nature* **407**, 496 (2000).
12. D. N. Lei, M. Zhang, B. H. Qu, L. B. Chen, Y. G. Wang, E. D. Zhang, Z. Xu, Q. H. Li and T. H. Wang, *Nanoscale* **4**, 3422 (2012).
13. T. C. Jiang, F. X. Bu, X. X. Feng, I. Shakir, G. L. Hao and Y. X. Xu, *ACS Nano* **11**, 5140 (2017).

14. X. L. Wu, Y. G. Guo, L. J. Wang and C. W. Hu, *J. Phys. Chem. C* **112**, 16824 (2008).
15. M. V. Reddy, G. V. Subba Rao and B. V. R. Chowdari, *Chem. Rev.* **113**, 5364 (2013).
16. H. S. Kim, Y. Piao, S. H. Kang, T. Hyeon and Y. E. Sung, *Electrochem. Commun.* **12**, 382 (2010).
17. Y. M. Lin, P. R. Abel, A. Heller and C. B. Mullins, *J. Phys. Chem. Lett.* **2**, 2885 (2011).
18. D. Cai, D. Li, L. X. Ding, S. Wang and H. Wang, *Electrochim. Acta* **192**, 407 (2016).
19. B. Wang, J. S. Chen, H. B. Wu, Z. Y. Wang and X. W. Lou, *J. Am. Chem. Soc.* **133**, 17146 (2011).
20. L. Zhang, H. B. Wu, S. Madhavi, H. H. Hng and X. W. Lou, *J. Am. Chem. Soc.* **134**, 17388 (2012).
21. H. J. Kim, K. I. Choi, A. Q. Pan, I. D. Kim, H. R. Kim, K. M. Kim, C. W. Na, G. Z. Cao and J. H. Lee, *J. Mater. Chem.* **21**, 6549 (2011).
22. W. Zhou, L. J. Lin, W. J. Wang, L. L. Zhang, Q. Wu, J. H. Li and L. Guo, *J. Phys. Chem. C* **115**, 7126 (2011).
23. X. J. Zhu, Y. W. Zhu, S. Murali, M. D. Stoller and R. S. Ruoff, *ACS Nano* **5**, 3333 (2011).
24. F. Guo, Y. Ye, Z. X. Yang, C. Y. Hong, L. Q. Hu, C. X. Wu and T. L. Guo, *Appl. Surf. Sci.* **270**, 621 (2013).
25. Y. Q. Zou, J. Kan and Y. Wang, *J. Phys. Chem. C* **115**, 20747 (2011).
26. X. D. Xu, R. G. Cao, S. Jeong and J. Cho, *Nano Lett.* **12**, 4988 (2012).
27. S. L. Chou, Y. D. Pan, J. Z. Wang, H. K. Liu and S. X. Dou, *Phys. Chem. Chem. Phys.* **16**, 20347 (2014).
28. J. Zheng, X. Yu, C. Wang, Z. Cao, H. Yang, D. Ma and X. Xu, *J. Mater. Sci. Mater. Electron.* **27**, 4457 (2016).
29. I. Kovalenko, B. Zdyrko, A. Magasinski, B. Hertzberg, Z. Milicev, R. Burtovyy, I. Luzinov and G. Yushin, *Science* **334**, 75 (2011).
30. X. Y. Zhao, M. H. Cao and C. W. Hu, *RSC Adv.* **2**, 11737 (2012).
31. C. Y. Wu, X. P. Li, W. S. Li, B. Li, Y. Q. Wang, Y. T. Wang, M. Q. Xu and L. D. Xing, *J. Power Sources* **251**, 85 (2014).
32. Q. Q. Wang, G. L. Zhao and G. R. Han, *Mater. Lett.* **59**, 2625 (2005).
33. Z. Wang, D. Luan, S. Madhavi, Y. Hu and X. W. Lou, *Energy Environ. Sci.* **5**, 5252 (2012).
34. X. Wang, Y. Xiao, C. W. Hu and M. H. Cao, *Mater. Res. Bull.* **59**, 162 (2014).
35. L. Hu, N. Yan, Q. W. Chen, P. Zhang, H. Zhong, X. R. Zheng, Y. Li and X. Y. Hu, *Chem. Eur. J.* **18**, 8971 (2012).
36. S. Bai, S. Q. Chen, X. P. Shen, G. X. Zhu and G. X. Wang, *RSC Adv.* **2**, 10977 (2012).
37. Q. Q. Xiong, T. P. Tu, X. Ge, X. L. Wang and C. D. Gu, *J. Power Sources* **274**, 1 (2015).
38. Q. Q. Xiong, S. J. Shi, H. Tang, X. L. Wang, C. D. Gu and J. P. Tu, *Mater. Res. Bull.* **61**, 83 (2015).
39. A. Banerjee, V. Aravindan, S. Bhatnagar, D. Mhamane, S. Madhavi and S. Ogale, *Nano Energy* **2**, 890 (2013).
40. D. H. Wei, J. W. Liang, Y. C. Zhu, Z. Q. Yuan, N. Li and Y. T. Qian, *Part. Part. Syst. Character.* **30**, 143 (2013).
41. B. Zhao, R. Z. Liu, X. H. Cai, Z. Jiao, M. H. Wu, X. T. Ling, B. Lu and Y. Jiang, *J. Appl. Electrochem.* **44**, 53 (2014).
42. S. Laruelle, S. Grugeon, P. Poizot, M. Dollé, L. Dupont and J.-M. Tarascon, *J. Electrochem. Soc.* **149**, A627 (2002).
43. S. Chaudhari and M. Srinivasan, *J. Mater. Chem.* **22**, 23049 (2012).
44. Y. Jiang, S. Chen, D. B. Mu, B. R. Wu, Q. Liu, Z. K. Zhao and F. Wu, *J. Mater. Sci.* **52**, 10950 (2017).